1   **A new high-performance proton-conducting electrolyte for next-generation**

2   **solid oxide fuel cells**

3   Nikdalila Radenahmad[1,2], Ahmed Afif[1], Abdalla M Abdalla[3], Muhammad Saqib[4], Jun-Young

4   Park[4], Juliana Zaini[1], John Irvine[5], Jung Hyun Kim[6], Abul K Azad[1*]

5   [1]*Faculty of Integrated Technologies, Universiti Brunei Darussalam, Jalan Tungku Link, Gadong*

6   *BE 1410, Brunei Darussalam*

7   [2]*Department of Chemical Engineering, Faculty of Engineering, Chulalongkorn University,*

8   *Bangkok, 10330, Thailand*

9   [3]*Mechanical Engineering Department, Faculty of Engineering, Suez Canal University, Ismailia*

10   *41522, Egypt*

11   [4]*Department of Nanotechnology and Advanced Materials Engineering, Sejong University, Seoul*

12   *143-747, Republic of Korea*

13   [5]*School of Chemistry, University of St Andrews, Fife KY16 9ST, UK*

14   [6]*Department of Advanced Materials Science and Engineering, Hanbat National University, 125,*

15   *Dongseo-daero, Yuseong-gu, Daejeon, 305-719, South Korea*

16

17   *Corresponding author's Email: abul.azad@ubd.edu.bn, Phone: +6737219025*

18

Abstract

20   Conventional solid oxide fuel cells (SOFCs) are operable at high temperatures (700 −

21   1,000 °C) with the most commonly used electrolyte, yttria-stabilized zirconia (YSZ). SOFC

22   R&D activities have thus been carried out to reduce the SOFC operating temperature. At

23   intermediate temperatures (400 - 700 °C), barium cerate ($BaCeO_3$) and barium zirconate

24   ($BaZrO_3$) are good candidates for use as proton-conducting electrolytes due to their promising

25   electrochemical characteristics. Here, we combined two widely studied proton-conducting

26   materials with two dopants and discovered an attractive composition for the investigation of

27   electrochemical behaviors. $Ba_{0.9}Sr_{0.1}Ce_{0.5}Zr_{0.35}Y_{0.1}Sm_{0.05}O_{3-\delta}$ (BSCZYSm), a perovskite-type

28   polycrystalline material, has shown very promising properties to be used as proton-conducting

29   electrolytes at intermediate temperature range. BSCZYSm shows a high proton conductivity of

1   4.167×10^{-3} S cm^{-1} in a wet argon atmosphere and peak power density of 581.7 mW cm^{-2} in Ni-

2   BSCZYSm | BSCZYSm | BSCF cell arrangement at 700 °C, which is one of the highest in

3   comparison to proton-conducting electrolyte-based fuel cells reported till now.

4   *Keywords:* Proton-conducting electrolyte, Structural analysis, Electrochemical performance,

5   Power density, Solid oxide fuel cells.

6

Introduction

8   In the search for green energy resources, solid oxide fuel cells (SOFCs) have become a

9   promising alternative since these materials are practicable in a variety of fuels and have low

10   emission [1–3]. The state-of-the-art oxide ion-conducting electrolyte for SOFCs is yttria-stabilized

11   zirconia (YSZ), which operates at high temperatures (700 – 1000 °C). The high operating

12   temperature is a challenge in material selection and complex technology, resulting in high costs

13   and delayed SOFC commercialization. Although using oxide ion conductors in SOFCs is typical

14   at high temperatures, the challenges are still obvious in terms of mismatched materials, low

15   tolerance to operating conditions and low fuel efficiencies. Intermediate-temperature (IT)-SOFCs

16   are becoming increasingly attractive for energy generation. At intermediate temperatures (400-

17   700 °C), several perovskite electrolytes (general formula, ABO_3) exhibit good electrochemical

18   properties in terms of proton conductivity [4–8]. Enhanced proton conduction is a promising

19   method to improve the performance in operation. Higher efficiency can be achieved in proton-

20   conducting SOFCs (SOFC-H$^+$) than in oxide ion conducting SOFCs (SOFC-O^{2-}), although the

21   maximum voltage and power density are still lower [9].

22   Since Iwahara et al. [10] discovered protonic conductivity in $SrCeO_3$ ceramic oxides,

23   doped $BaCeO_3$ and doped $BaZrO_3$ have been extensively investigated as electrolyte materials for

24   proton-conducting SOFCs (SOFC-H$^+$) [4,11–14]. Yttrium-doped $BaCeO_3$ has been found to be one

25   of the best proton conductors but is unstable in CO_2- and H_2O-containing atmospheres. On the

26   other hand, $BaZr_{0.9}Y_{0.1}O_{3-\delta}$ shows excellent stability in CO_2- and H_2O-containing atmospheres,

27   but its protonic conductivity is not sufficient for practical applications [15–17]. As there is a trade-

28   off between conductivity and chemical stability, solid solutions between $BaCeO_3$ and $BaZrO_3$,

29   e.g., $Ba(Ce_{0.7}Zr_{0.1}Y_{0.2})O_{3-\delta}$, have been found to possess a high ionic conductivity of 9×10^{-3} at

30   500 ºC and to show excellent chemical stability in a 2% CO_2 atmosphere at 500 ºC (stored for

one week) and in an H_2O vapor atmosphere. Co-doping of the B-site (Ce/Zr site) with two different trivalent cations is very beneficial for achieving high proton conductivity and good stability in humid atmospheres [18,19]. Several dopants have been studied to improve the stability and conductivity of these materials. The A-site of perovskite can be doped with a large-ionic-radius element, and the B-site can be doped with a small-ionic-radius element [6]. In most previous works, some percentage of Ce and/or Zr was substituted by trivalent cations such as Y, Yb, Gd, Sc, Pr, and Sm at the B-site to generate oxygen vacancies to enhance the conductivity of the material [20–24]. For example, Ce was doped with Zr in a $BaCe_{0.9-x}Zr_xY_{0.1}O_{2.95}$ series to increase proton conductivity and chemical stability, resulting in good chemical stability in steam and carbon dioxide atmospheres [22,23]. The percentage of Ce at the B-site also has a strong effect on the proton concentration in perovskite materials[25]. Sm-doped proton conductors show promising performance for IT-SOFCs. Very little work has been done to substitute Ba with Sr or Ca, which can also have a good effect on protonic conductivity [26].

In this work, we prepared a novel composite electrolyte of $Ba_{0.9}Sr_{0.1}Ce_{0.5}Zr_{0.35}Y_{0.1}Sm_{0.05}O_{3-\delta}$ (BSCZYSm) and carried out X-ray diffraction (XRD), Rietveld refinement, particle size analysis, thermogravimetric analysis (TGA), electrochemical impedance spectroscopy (EIS), fuel cell tests and scanning electron microscopy (SEM). An anode-supported fuel cell with a thick anode layer and thinner electrolyte and cathode layers was fabricated. A thin electrolyte is important to decrease the ohmic loss, thus increasing performance and decreasing the operating temperature, which diminishes the degradation and prolongs the lifetime of the cell. $Ba_{0.5}Sr_{0.5}Co_{0.8}Fe_{0.2}O_{3-\delta}$ (BSCF) is an excellent mixed ionic-electronic conductor (MIEC) for IT-SOFC application because of its superior electrochemical characteristics relative to other cathodes with a perovskite structure (ABO_3) [27]. BSCF has a high oxygen diffusion rate and oxygen vacancy concentration, resulting in an effective oxygen reduction reaction (ORR) and high power production [28]. Hence, we examined the novel electrolyte (BSCZYSm) and fabricated an anode-supported fuel cell with BSCF as a cathode to observe the electrochemical characteristics.

Methods

Synthesis and characterizations of BSCZYSm

$Ba_{0.9}Sr_{0.1}Ce_{0.5}Zr_{0.35}Y_{0.1}Sm_{0.05}O_{3-\delta}$, a perovskite-type material, was prepared by the solid-state reaction method. Stoichiometric amounts of $BaCO_3$, SrO, CeO_2, ZrO_2, Y_2O_3 and Sm_2O_3 powders were mixed in ethanol and ground using an agate mortar and pestle. The mixed powders were sintered in air at 950 °C for 8 hours. A hydraulic press was utilized to make 13 mm diameter pallets by pressing at 4 psi and sintering at 1400°C and 1450°C for 6 hours and 8 hours, respectively. XRD patterns were obtained on an Empyrean Alpha 1 X-ray diffractometer from Malvern Panalytical (CuKα1, λ = 1.5406 Å) in air, and Rietveld analysis was performed using FullProf software [29]. Particle size analysis was carried out using a HORIBA particle size analyser to specify the grain size of the particle after manual grinding of the prepared material with a mortar and pestle for 10-15 minutes. The hydration furnace was operated at 0.4 P_{N_2} at 800 °C, 600 °C, 400 °C, 200 °C and 150 °C with dwelling times of 2 hours, 2 hours, 48 hours, 2 hours and 55 hours, respectively. The heating and cooling rates were 200 °C/hour to reach 400 °C and 10 °C/h for cooling to 150 °C. The hydrated samples were prepared to examine the chemical and thermal stability and proton intake capacity by using a NETZSCH thermogravimetric analyser operated under a 20 ml/min constant flow of nitrogen. Pt paste was painted on both sides of a 13 mm diameter pellet and sintered at 1000 °C for 2 hours. Impedance spectroscopy was carried out by Solartron 1260 impedance analyzer in the frequency range of 100 mHz - 6 MHz and 1 V rms in signal amplitude from 1000 °C to 150 °C with the step of 50 °C at Chalmers University of Technology. This experiment was operated in wet and dry Argon atmosphere. ZView (Scribner Associates Inc.) software was utilized to examine impedance data for analyzing conductivity.

Fabrication and performance test of fuel cells

The fuel cell performance test was carried out at Sejong University, South Korea. The anode supported cell, $NiO-Ba_{0.9}Sr_{0.1}Ce_{0.5}Zr_{0.35}Y_{0.1}Sm_{0.05}O_{3-\delta}$ (BSCZYSm) | BSCZYSm | $Ba_{0.5}Sr_{0.5}Co_{0.8}Fe_{0.2}O_{3-\delta}$ (BSCF) as anode, electrolyte and cathode, was assembled. Anode layer was made from mixing NiO (65 wt%), BSCZYSm (35 wt%), Solsperse, corn starch and ethanol then ball milled with zirconia balls for 1 day. The ball milling rate was as low as 187 rpm.

Hence, the chance of getting impurities after milling is zero because firstly we use fresh zirconia balls and secondly the milling rate was not so high so that does not cause any structural deformation.
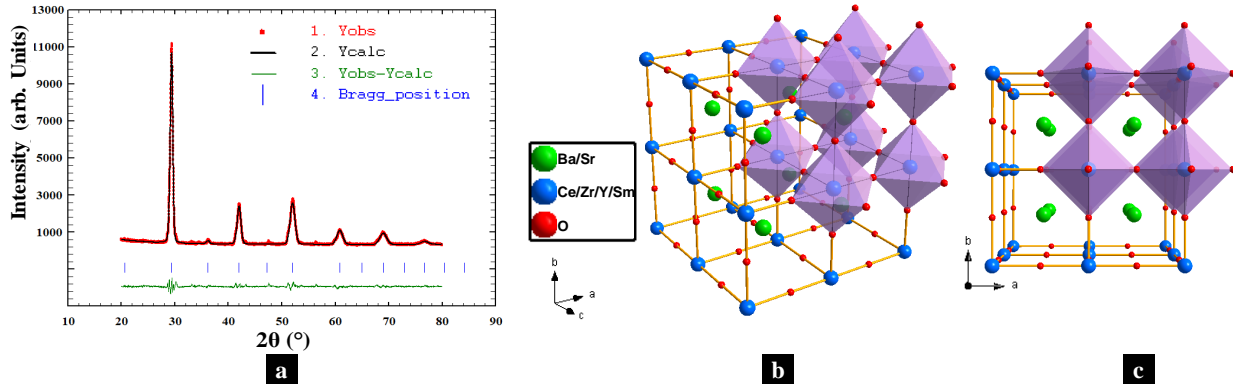
The mixture was dried and pressed at 2 tons for 1 minute to make pellets for sintering at 900 °C for 2 hours. Anode functional layer (AFL) was prepared by mixing NiO (65 wt%), BSCZYSm (35 wt%), Solsperse and ethanol by ball milling for 1 day. The slurry was added with Di-n-butyl phthalate (DBP) and polyvinyl butyral (PVB, B-98, Butvar) on the next day and ball milled for one day. A side of the sintered anode was coated by AFL by drop coating and sintered at 400 °C for 2 hours. Electrolyte slurry was made from mixing BSCZYSm, Solsperse and ethanol by ball milling for one day. The slurry was added with DBP and Butvar on the next day and continued ball milling for one day. The anode with AFL was coated with electrolyte by dropping. The electrolyte layered cell was sintered at 1450 °C for 4 hours which was the final sintering temperature of the electrolyte. The BSCF cathode (60 wt%) was made into ink by mixing with BSCZYSm (40 wt%) and texanol. The cathode was painted on the cell with an area of 0.2552 cm^2 ($\pi(0.285 \text{ cm})^2$) and sintered at 1,000 °C for 4 hours. The cathode area was pasted with platinum paste and attached with silver mesh and gold wire. The fuel cell was connected with the gold wire of the test station and placed on the alumina jig where the anode was at the bottom side and the cathode was at the top. Ceramabond (100% Ceramabond-668, USA) was used to seal the cell with the jig and close the gap to prevent gas mixing. Ceramabond-668, a high temperature one-part alumina-silica based adhesive, was bought from Aremco.com (an USA based commercial company). Ceramabond-668 is an excellent for heaters. It can make bonds and seals ceramics to ceramics and ceramics to metals in applications up to 2500°F (1371°C). At the anode, nitrogen gas was fed at 200 standard cubic centimeter per minute (sccm) followed by feeding nitrogen/hydrogen (150/50 sccm, 100/100 sccm) and finally pure hydrogen of 200 sccm while cathode was fed with an air of 200 sccm. The voltage, current and impedance of fuel cell at 700 ℃, 650 ℃ and 600 ℃ were recorded by the Potentiostat instrument of Bio-Logic SP-240. The impedance was collected in a frequency range of 0.1 Hz - 1 MHz with a signal amplitude of 10 mV under open-circuit voltage (OCV). The impedance spectra were fitted with an equivalent circuit using EC-Lab software to calculate conductivity. Scanning electron images from Hitachi SU8010 Field Emission scanning electron microscope (FE-SEM) was used to examine the fuel cell micro-feature.

Results and discussion

X-ray diffraction

Fig. 1a) shows the Rietveld refinement of the XRD data of the BSCZYSm electrolyte material. Indexing of the pattern was performed using TREOR90 software, and subsequent refinement of cell parameters was performed by using Checkcell. The Rietveld refinement shows that BSCZYSm crystallizes in the cubic symmetry (*Pm-3m* space group), and a schematic 3D structure is shown in Fig. 1b) and c). In the perovskite ABO_3 structure, the central green atom represents the A-site, the central blue atom of each octahedral BO_6 represents the B-site, and the small red atom represents the O-site. The observed lattice parameter of 4.305 Å was smaller than that of $BaCeO_3$ (a = 4.445 Å) [30] but larger than that of $BaZrO_3$ (a = 4.193 Å) [31]. The phase structure of $BaCeO_3$-$BaZrO_3$ is highly dependent on the concentration of Ce/Zr at the B-site. Typically, Y-doped $BaCeO_3$ is orthorhombic, and Y-doped $BaZrO_3$ is cubic. In fact, different doped $BaCeO_3$ samples can have different symmetry and cell parameters depending on the B-site cation ratio, synthesis route and final sintering temperature. $BaCe_{0.9-x}Zr_xY_{0.1}O_{3-\delta}$ shows an orthorhombic structure for x = 0.1 and 0.2 and a cubic structure for $x \geq 0.3$ [23]. When the Y percentage is slightly higher, e.g., $BaCe_{0.8-x}Zr_xY_{0.2}O_{3-\delta}$, the phase structure is orthorhombic for x = 0.1 - 0.5 and cubic for x = 0.6 - 0.8 [22]. Sm- and Y-doped $BaCeO_3$ also shows an orthorhombic crystal structure[32]. Since the ionic radii of Y^{3+} and Sm^{3+} in 6-coordinate polyhedral, 0.90 Å and 0.958 Å, are very close to each other, the small percentage of Y and Sm co-doped $Ba_{0.9}Sr_{0.1}Ce_{0.5}Zr_{0.35}Y_{0.1}Sm_{0.05}O_{3-\delta}$ shows cubic symmetry depending on the Ce/Zr concentration. These studies show the influence of the preparation procedure and sintering temperatures on the crystalline structure of the obtained materials. Higher sintering temperatures, which are normally used for solid-state reactions, have an important effect on the symmetry of the crystal structure. $Ba_{0.9}Sr_{0.1}Ce_{0.5}Zr_{0.35}Y_{0.1}Sm_{0.05}O_{3-\delta}$ and $Ba_{0.5}Sr_{0.5}Co_{0.8}Fe_{0.2}O_{3-\delta}$ were mixed and sintered at 1000 °C for 4 hours, and then XRD data were collected. XRD confirmed that the electrolyte and cathode did not react with each other, as no additional phase was detected, which shows the compatibility of the electrolyte and cathode in fuel cell operation. The XRD profiles of mixed $Ba_{0.9}Sr_{0.1}Ce_{0.5}Zr_{0.35}Y_{0.1}Sm_{0.05}O_{3-\delta}$ and $Ba_{0.5}Sr_{0.5}Co_{0.8}Fe_{0.2}O_{3-\delta}$ are shown in Fig. 2.

**Fig. 1** a) Rietveld refinement profile of $Ba_{0.9}Sr_{0.1}Ce_{0.5}Zr_{0.35}Y_{0.1}Sm_{0.05}O_{3-\delta}$, where the observed data are represented by dots and the calculated data are represented by the continuous line. The short vertical lines represent the position of the Bragg reflections. The bottom line shows the difference of the plots ($I_{ob}-I_{calc}$), b) the 3D diagram of the perovskite (ABO_3) structure drawn by Diamond software in overall view and c) front view.
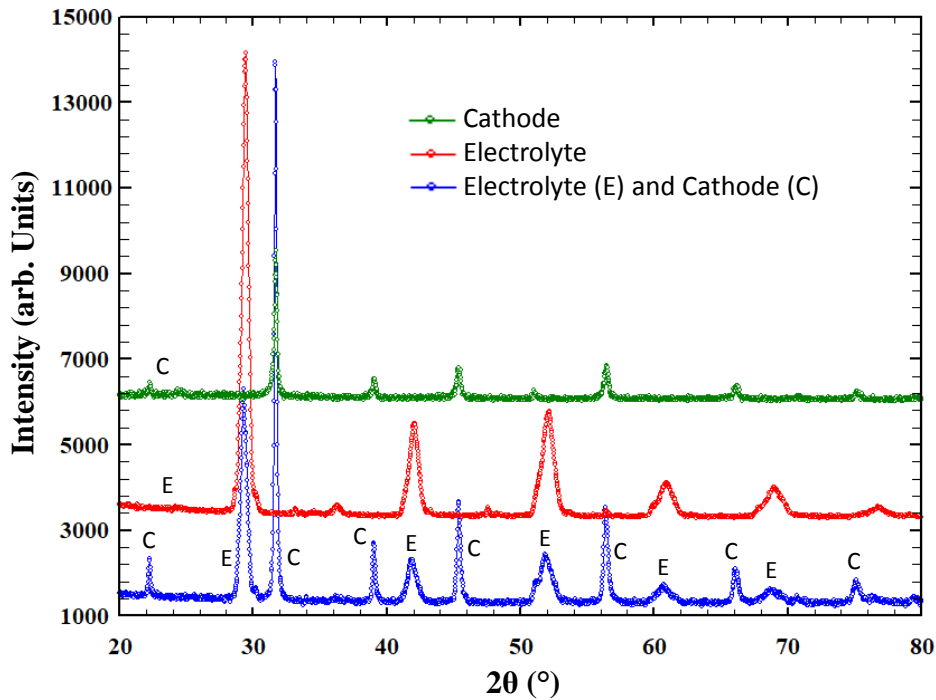
Fig. 2 The XRD profiles of pure BSCF cathode, pure BSCZYSm electrolyte and BSCZYSm-BSCF.

1   *Particle size analysis*
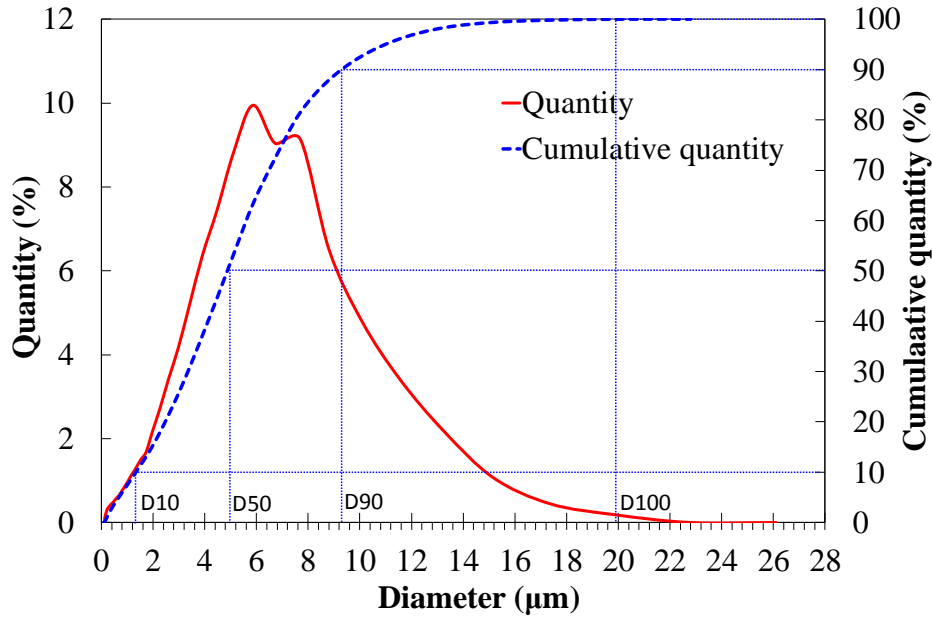
2
3   **Fig. 3** Particle size distribution of $Ba_{0.9}Sr_{0.1}Ce_{0.5}Zr_{0.35}Y_{0.1}Sm_{0.05}O_{3-\delta}$.

4

5   **Table 1** Particle size at various D-values of $Ba_{0.9}Sr_{0.1}Ce_{0.5}Zr_{0.35}Y_{0.1}Sm_{0.05}O_{3-\delta}$.

D-value	Particle size (µm)
D10	1.341
D50	4.878
D90	9.367
D100	19.90

6

7   The particle size distribution of $Ba_{0.9}Sr_{0.1}Ce_{0.5}Zr_{0.35}Y_{0.1}Sm_{0.05}O_{3-\delta}$ is shown in Fig. 3. The

8   powder sample was analysed after grinding with an agate mortar and pestle for 10-15 minutes.

9   Table 1 exhibits the particle size distribution in terms of the amount of particle. The particle size

10   of BSCZYSm has a median of 4.8674 µm, a mean of 5.195 µm and a mode of 5.490 µm. The D-

11   values represent the diameter of the particles indicated by a percentage. Overall, 10% of the

12   particles have a size smaller than 1.341 µm, and all other particles have a size not larger than

13   19.90 µm. However, the particle size of the material can be controlled during material

14   preparation by optimizing the ball milling time and sintering temperature, which can reduce the

15   porosity of the electrolyte material.

1

Thermogravimetric analysis

TGA was performed using the as-prepared and hydrated samples in the temperature range of 20 – 1000 °C, as shown in Fig. 4. As the samples consist of moisture (water) by nature and as a result of the hydration process, the moisture level is affected by elevated temperature, resulting in a weight change. Oxygen is a component of water; hence, this weight loss results in a change in oxygen occupancy (3-δ). Oxygen vacancies were created by doping trivalent cations (Y and Sm) at the B-site. For the as-prepared sample, the mass slightly increased at the beginning due to the adsorption of gas and subsequently decreased by 0.5% at 1000 °C, which is equivalent to an oxygen deficiency of 0.093 (oxygen occupancy of 2.907). In contrast, for the hydrated sample, the mass loss was 0.425% at 1000 °C, which is equivalent to an oxygen deficiency of 0.079 (oxygen occupancy of 2.921). Hence, TGA was used to examine the oxygen vacancy concentration. The oxygen occupancy of the hydrated material, 2.921, is closer to the theoretical oxygen occupancy (3 − δ = 2.925). For the hydrated sample, the mass loss indicates the loss of the proton that was absorbed during the hydration process in the atomic structure by forming an O-H bond. Hence, the mass loss of the hydrated sample represents the proton level, which is less than that of the as-prepared sample. The location of protons in the structure can be observed from neutron diffraction experiments [33,34].
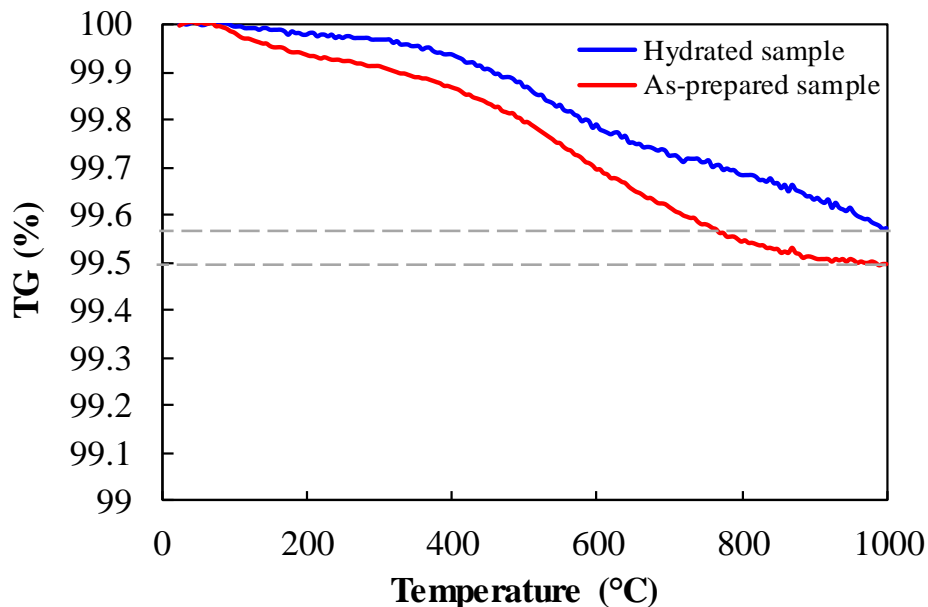

Fig. 4 Thermogravimetric profile of as-prepared and hydrated $Ba_{0.9}Sr_{0.1}Ce_{0.5}Zr_{0.35}Y_{0.1}Sm_{0.05}O_{3-\delta}$.

1 *Electrochemical impedance spectroscopy*

2   Fig. 5 shows the Arrhenius plots of the total conductivity of

3 $Ba_{0.9}Sr_{0.1}Ce_{0.5}Zr_{0.35}Y_{0.1}Sm_{0.05}O_{3-\delta}$ pellets in wet and dry argon in the temperature range of 400 –

4 700 °C in comparison with the conductivities of other similar proton conductors. BSCZYSm

5 exhibits notable electrochemical behavior, with a higher conductivity, 4.17×10^{-3} S cm^{-1} at 700

6 °C in wet Ar, and lower activation energy than the sample under dry conditions. This difference

7 is because of the introduced water in the wet experiment, which enhances proton conductivity.

8 The small activation energy is a favorable property that indicates the proton conduction ability of

9 the ceramic oxide. Table 2 shows the conductivity values and activation energies of BSCZYSm

10 in wet and dry Ar. At high temperatures, protons in proton-conducting perovskites are expected

11 to follow the Grotthuss mechanism [35] and transport in the following steps: i) a proton is

12 associated with a fixed oxygen atom; ii) the proton-oxygen bond reorients under the influence of

13 the neighboring oxygen atoms; iii) the proton starts to oscillate between the two oxygen atoms

14 and eventually moves to the neighboring oxygen [9]. The binding energy between OH$^\bullet$ and $M_{B'}$

15 varies with the dopant. Simulation results show that the binding energies of OH$^\bullet$-$M_{B'}$ (hydroxyl–

16 dopant pairs at the nearest neighbor sites) for Y, Yb and In were -0.26, -0.35 and -0.58 eV,

17 respectively, which is in good agreement with the experimental results [36]. A more stable state

18 for the hydroxyl-dopant pair will be found for a more negative value of the binding energies. A

19 report on substitution of Sr for Ba in $Ba_{1-x}Sr_xCe_{0.6}Zr_{0.2}Y_{0.2}O_{3-\delta}$ (x = 0.0 - 1.0) shows that a higher

20 conductivity was achieved by $Ba_{1-x}Sr_xCe_{0.6}Zr_{0.2}Y_{0.2}O_{3-\delta}$ (x = 0.3) than by $Ba_{1-x}Sr_xCe_{0.6}Zr_{0.2}Y_{0.2}O_{3-\delta}$ (x = 0.0), indicating that the small amount of Sr can enhance conductivity

22 [37].

T (°C)
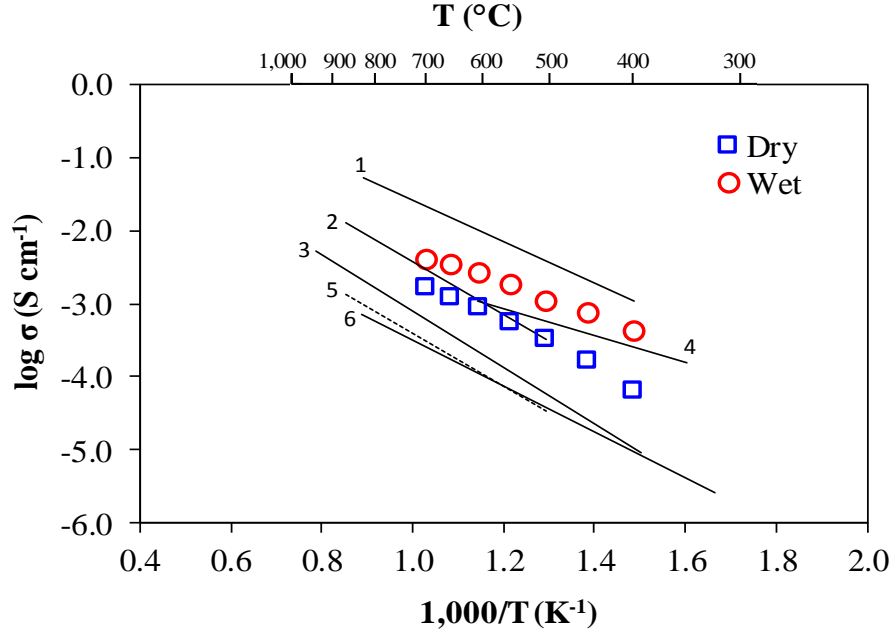
**Fig. 5** Conductivity versus temperature plots of $Ba_{0.9}Sr_{0.1}Ce_{0.5}Zr_{0.35}Y_{0.1}Sm_{0.05}O_{3-\delta}$ in the range of 400-700 °C in wet and dry argon atmospheres. Our results (circle, O; square, □) were compared with the conductivities of 1) $(Ba_{0.6}Sr_{0.4})(Ce_{0.75}Zr_{0.10}Y_{0.15})O_{3-\delta}$ in wet Ar [38], 2) $BaCe_{0.9}Nd_{0.1}O_{3-\delta}$ [39], 3) $BaCe_{0.7}Zr_{0.2}Y_{0.05}Zn_{0.05}O_3$ in wet Ar [40], 4) $BaZr_{0.8}Yb_{0.2}O_{3-\delta}$ in wet N_2 [41], 5) $Sr_{0.995}Ce_{0.95}Y_{0.05}O_{3-\delta}$ [39] and 6) $BaCe_{0.45}Zr_{0.45}Sc_{0.1}O_{3-\delta}$ in wet H_2 [18].

Table 2 Conductivities of $Ba_{0.9}Sr_{0.1}Ce_{0.5}Zr_{0.35}Y_{0.1}Sm_{0.05}O_{3-\delta}$ in wet and dry Ar atmospheres at different temperatures.

Temperature (°C)	Conductivity (S cm^{-1})	
	Wet Ar	**Dry Ar**
400	4.16×10^{-4}	6.43×10^{-5}
450	7.90×10^{-4}	1.66×10^{-4}
500	1.11×10^{-3}	3.31×10^{-4}
550	1.86×10^{-3}	5.68×10^{-4}
600	2.67×10^{-3}	9.16×10^{-4}
650	3.45×10^{-3}	1.23×10^{-3}
700	4.17×10^{-3}	1.71×10^{-3}
S.D.	1.42×10^{-3}	6.03×10^{-4}
Activation energy (eV) at 400 - 700 °C	0.44	0.61

11
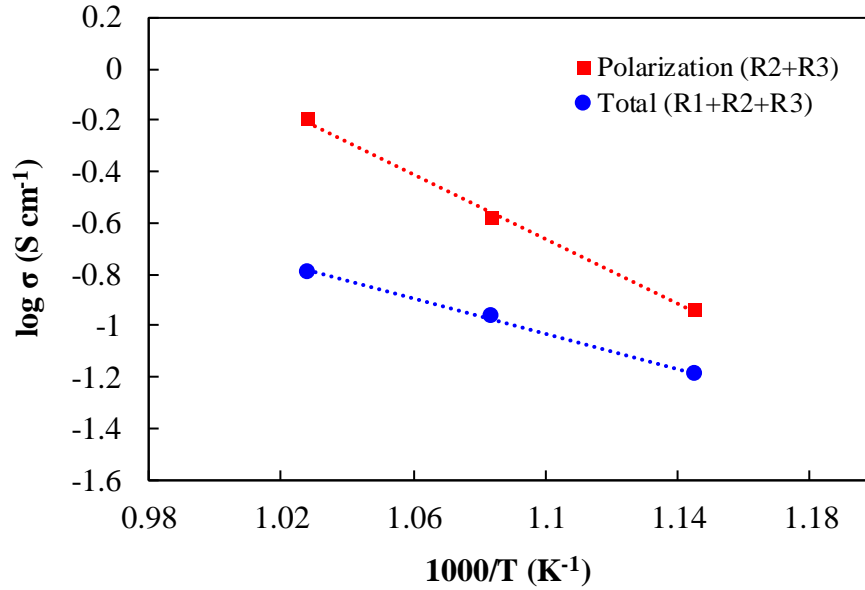
1
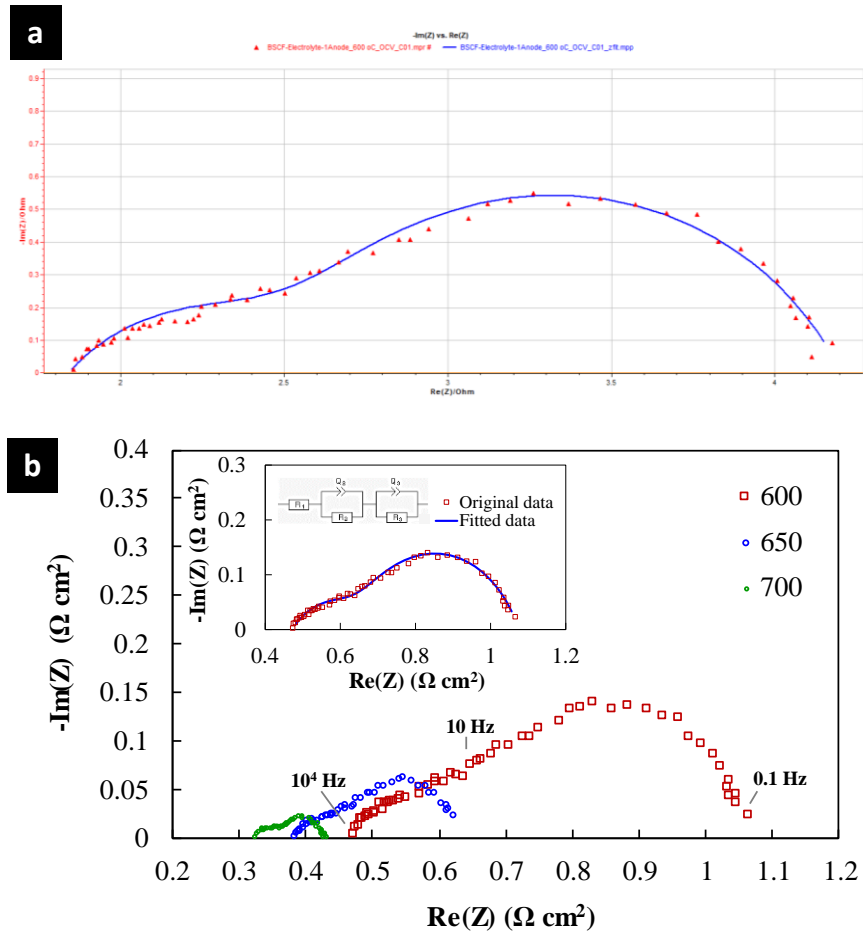
Fig. 6 Electrochemical impedance spectra of fuel cells at elevated temperatures in a) the original plot of the sample at 600 °C from EC lab and b) the area specific resistance. The fitting of the electrochemical impedance spectra with the equivalent circuit at 600 °C is shown in the insert.

1

2   **Fig. 7** Arrhenius plot of polarization and total conductivity of fuel cells at elevated temperatures.

3

4   Fig. 6a) shows the original impedance of the sample at 600 °C and Fig. 6b) presents the area

5   specific resistance (ASR) of the fuel cell at 600 - 700 °C, and the impedance was recorded after

6   the I-V measurement. At all temperatures, the first intercept represent the ohmic resistance (R_o)

7   at a high frequency, which is correlated with the ionic resistance of the electrolyte and attributed

8   to resistance at the interface of the electrode and electrolyte. The impedance spectra are

9   attributed to electrochemical reaction or polarization resistance (R_p), which can be identified at i)

10   the medium-frequency range of ~10 – 10^4 Hz involving the charge transfer mechanism of the

11   oxygen ion and electron and ii) the low-frequency range of ~0.1 – 10 Hz related to the oxygen

12   ion and mass transfer mechanism owing to the diffusion of the oxygen ions [42], [43]. The obtained

13   impedance at 600 °C was explained by an equivalent circuit where the ohmic resistance (R_1) is in

14   parallel with two sub-circuits of polarization resistance (R_2 or R_3) and a constant phase element

15   (Q_2 or Q_3), as shown in the insert of Fig. 6b). The R_o of fuel cell is attributed to electrolyte

16   resistance, with values of 0.47 (0.077), 0.37 (0.077) and 0.32 (0.077) Ω cm^2 at 600, 650 and 700

17   °C, respectively, while the cell exhibited R_p values of 0.60 (0.253), 0.27 (0.253) and 0.11 (0.253)

18   Ω cm^{2}at 600, 650 and 700 °C, respectively. A greater porosity of the electrode microstructure is

19   essential to achieve a lower R_p for cell performance enhancement [44]. The smallest impedance at

20   700 °C patently denotes the highest conductivity. Impedance fitting of the sample was performed

21   to determine the subsequent resistivity by conductivity calculations. The conductivities are

1   plotted in Fig. 7 according to the linear Arrhenius relation, where the highest conductivity was at

2   700 °C and the lowest conductivity was at 600 °C under the same conditions. The fuel cell

3   exhibited total conductivities of 0.06 (0.049), 0.11 (0.049) and 0.16 (0.049) S cm^{-1} at 600, 650

4   and 700 °C, respectively, while the polarization conductivities were 0.12 (0.274), 0.26 (0.274)

5   and 0.64 (0.274) S cm^{-1} at 600, 650 and 700 °C, respectively. The polarization conductivities

6   were higher than the total conductivity because the total conductivities consisted of ohmic and

7   polarization resistance in the calculation, where ohmic resistance was affected by the electrolyte

8   resistance.

9

10 *Fuel cell performance*

11   BSCZYSm was further investigated as the electrolyte material in a complete fuel cell.

12 The cell was fabricated with a configuration of Ni-BSCZYSm | BSCZYSm | BSCF as the anode,

13 electrolyte and cathode. The cell was exposed to 200 sccm hydrogen as the fuel and 200 sccm air

14 as an oxidant at 600 - 700°C. Fig. 8 shows the voltage and power density versus current density

15 trends of the cells. The data were collected after the OCV was stabilized at 700 °C, which is

16 attributed to the appropriate mass transport property and good sealing of the fuel cell [42]. The

17 cell exhibited a maximum power density of 581.7 mW/cm^2 at 700 °C with an OCV of 1.025 V

18 and a power density of 327.8 mW/cm^2 at 600 °C with an OCV of 1.04 V. The cell performance

19 at 700 °C shows a higher power density than the reported values from similar cells, as shown in

20 Table 3. The obtained OCVs are in the range of 1.025 to 1.04 V. The increase in temperature

21 plays an important role in accelerating the electrochemical reaction, which decreases the OCV

22 consistent with the Nernst equation [45]. The obtained high OCV proved that the electrolyte is

23 dense, serving as a membrane to prevent gas leakage from the anode to the cathode or vice versa.

24 As the maximum power density is proportional to OCV^2, a high OCV could directly benefit the

25 performance [46]. The power density could be enhanced for greater performance by reducing the

26 ohmic resistance of the electrolyte and the polarization resistance of the electrodes, which

27 facilitates high ionic conductivity through the electrolyte [47]. A reduction in the thickness of the

28 electrolyte is also a key to enhancing performance [48]. The fuel cell operation of Ni-BSCZYSm |

29 BSCZYSm | BSCF released water at the cathode gas outlet, which proved that the proton-

30 conducting mechanism was dominant in this experiment at the examined temperature of 600 –

1 700 °C. According to the reported values in Table 3, the fuel cell performance varies with the

2 material selection; precursor preparation method; heat treatment temperature of the material;

3 fabrication of the fuel cell; layer multiplication of the anode, electrolyte or cathode; etc. A

4 commonly used cell fabrication method is the typical dry-pressing anode substrate preparation,

5 where the anode is fired alone or co-pressed and co-fired with the electrolyte layer, followed by

6 painting of the cathode slurry onto the electrolyte layer [49–51]. Other cell fabrication methods

7 have also been applied, such as tape casting, gel casting, phase inversion for anode preparation,

8 spin coating, solution coating, pressurized spray coating of the electrolyte onto the anode layer

9 and screen printing or painting of the cathode onto the electrolyte layer. In this report, we used a

10 typical dry-pressing method to prepare the anode substrate, which revealed the greatest

11 performance at 700 °C compared to the reported values based on dry-pressed anodes. However,

12 Nguyen and Yoon [52] applied a spin-coating process to deposit an electrolyte onto the anode, and

13 this process seems to be a better approach for controlling the electrolyte thickness to achieve

14 higher performance. It is now evident that NiO can diffuse from anode to electrolyte and might

15 change the sintering nature as well as conductivity of the materials [53]. We haven't used NiO as

16 sintering aid of any of the materials and haven't observed any tress of Ni in the electrolyte.

17
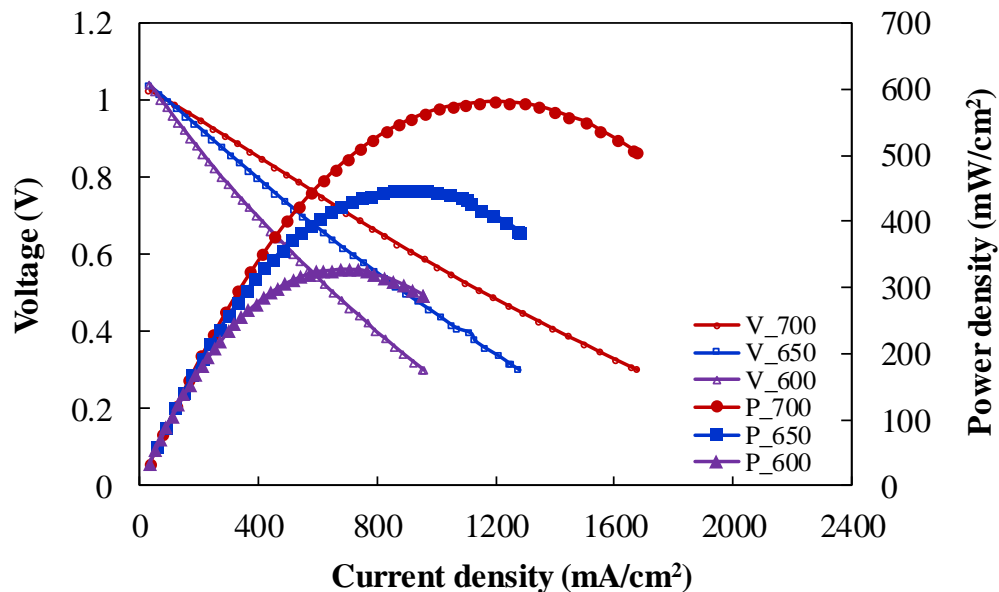
18

19 **Fig. 8** Voltage and power density versus current density curves of the Ni-BSCZYSm |

20 BSCZYSm | BSCF single cell at 600, 650 and 700 °C.

21

15

1   **Table 3** Comparison of power density and OCV of Ni-BSCZYSm | BSCZYSm | BSCF cells

2   with those of some reported fuel cells in the literature.

Cell	Power density $(\mathrm{mWcm^{-2}})$	Temperature (°C)	OCV (V)	Reference
NiO- $Ba_{0.9}Sr_{0.1}Ce_{0.5}Zr_{0.35}Y_{0.1}Sm_{0.05}O_{3-\delta}$(BSCZYSm)‖BSCZYSm‖$Ba_{0.5}Sr_{0.5}Co_{0.8}Fe_{0.2}O_{3-\delta}$	327.8	600	1.04	Present study
	448.8	650	1.035	
	581.7	700	1.025	
NiO-$BaZr_{0.1}Ce_{0.7}Y_{0.2}O_{3-\delta}$ ‖ $BaZr_{0.3}Ce_{0.5}Y_{0.2}O_{3-\delta}$ ‖ $Sm_{0.5}Sr_{0.5}CoO_{3-\delta} - Ce_{0.8}Sm_{0.2}O_{2-\delta}$ (SSC–SDC)	396	600	1.02	[9]
	513	650	1.01	
NiO-$BaZr_{0.1}Ce_{0.7}Y_{0.1}Yb_{0.1}O_{3-\delta}$ (BZCYYb) ‖ BZCYYb ‖ BZCYYb-LSCF	470*	600	1.07*	[52]
	590*	650	1.04*	
	710*	700	1.00*	
	1000	750	0.94	
Ni– $BaZr_{0.1}Ce_{0.7}Y_{0.2}O_{3-\delta}$(BZCY) ‖ $BaCe_{0.7}In_{0.2}Yb_{0.1}O_{3-\delta}$ ‖ $La_{0.6}Sr_{0.4}Co_{0.2}Fe_{0.8}O_{3-\delta}$ (LSCF) – BZCY	150	600	0.984	[54]
	218	650	0.981	
	280	700	0.963	
Ni–$BaZr_{0.1}Ce_{0.7}Y_{0.1}Yb_{0.1}O_{3-\delta}$ (BZCYYb) ‖ BZCYYb ‖ $La_{0.6}Sr_{0.4}Co_{0.2}Fe_{0.8}O_{3-\delta}$ (LSCF)– BZCYYb	260	600	1.01	[55]
Ni-$BaZr_{0.1}Ce_{0.7}Y_{0.1}Yb_{0.1}O_{3-\delta}$ (BZCYYb) ‖ BZCYYb ‖ $PrBaCo_2O_{5+\delta}$ (PBCO)	223	600	1.016	[56]
	358	650	1.007	
	490	700	0.983	
Ni-$BaZr_{0.1}Ce_{0.7}Y_{0.1}Yb_{0.1}O_{3-\delta}$ (BZCYYb) ‖ BZCYYb ‖ $PrBaFe_2O_{5+\delta}$ (PBFO)	179	600	1.034	[57]
	302	650	1.015	
	452	700	1.006	

NiO−ScSZ || ScSZ || $La_{0.8}Sr_{0.2}Sc_yMn_{1-y}O_{3-\delta}$ (y = 0.0–0.2)	80 (y = 0) 200 (y = 0.05)	650		[58]
$BaCe_{0.5}Zr_{0.3}Y_{0.16}Zn_{0.04}O_{3-\delta}$ (BCZYZ) – NiO || BCZYZ ||$LaSr_3Co_{1.5}Fe_{1.5}O_{10-\delta}$ (LSCF)	175 250 275	600 650 700	1.02 1.00 0.95	[59]
NiO–$BaCe_{0.5}Zr_{0.3}Y_{0.16}Zn_{0.04}O_{3-\delta}$ (BCZYZ) || BCZYZ || $Sm_{0.5}Sr_{0.5}CoO_{3-\delta}$ (SSC) – BCZYZ	246 364 528	600 650 700	1.049 1.039 1.015	[60]
Ni- $BaCe_{0.5}Zr_{0.3}Y_{0.16}Zn_{0.04}O_{3-\delta}$ (BCZYZ) || BCZYZ || $PrBaCo_2O_{5+\delta}$ (PBCO)	194 266 361	600 650 700	1.042 1.021 1.007	[61]
Ni–$BaCe_{0.5}Zr_{0.3}Y_{0.16}Zn_{0.04}O_{3-\delta}$(BCZYZ) || BCZYZ || $Ba_{0.5}Sr_{0.5}Zn_{0.2}Fe_{0.8}O_{3-\delta}$(BSZF)–BCZYZ	201 323 387	600 650 700	1.042 1.021 1.007	[62]
Ni-$BaZr_{0.1}Ce_{0.7}Y_{0.2}O_{3-\delta}$(BZCY7) || BZCY7 || $Ba_{0.5}Sr_{0.5}Zn_{0.2}Fe_{0.8}O_{3-\delta}$ (BSZF) -BZCY7	277 415 486	600 650 700	1.062 1.041 1.015	[63]
Ni–$BaCe_{0.5}Zr_{0.3}Y_{0.16}Zn_{0.04}O_{3-\delta}$(BCZYZ) || BCZYZ || $GdBa_{0.5}Sr_{0.5}Co_2O_{5+\delta}$(GBSC)	210 290 350	600 650 700	1.044 1.024 1.009	[64]
NiO-$BaCe_{0.5}Zr_{0.3}Y_{0.2}O_{3-\delta}$ (BCZY) -Z-C_2-starch || NiO-BCZY-Z-C_2 || BZCY-Z-C_2 || $Ba_{0.5}Sr_{0.5}Co_{0.8}Fe_{0.2}O_{3-\delta}$ (BSCF)	102 190* 237* 302	500 600 650 700	1.094 1.014	[65]
NiO-$BaCe_{0.5}Zr_{0.3}Y_{0.16}Zn_{0.04}O_{3-\delta}$ (BCZYZ) || BCZYZ ||	178 242	600 650	1.021 1.015	[66]

SmBa$_{0.5}$Sr$_{0.5}$Co$_2$O$_{5+\delta}$ (SBSC)	306	700	1.007	
NiO– BaCe$_{0.5}$Zr$_{0.3}$Y$_{0.16}$Zn$_{0.04}$O$_{3-\delta}$ (BZCYZn) ‖ BZCYZn ‖ SrCo$_{0.9}$Sb$_{0.1}$O$_{3-\delta}$ (SCS)	241 281 364	600 650 700	1.005 0.992 0.987	[67]
NiO–BaCe$_{0.5}$Zr$_{0.3}$Y$_{0.16}$Zn$_{0.04}$O$_{3-\delta}$ (BCZYZn) ‖ BCZYZn ‖ Ba$_{0.5}$Sr$_{0.5}$Zn$_{0.2}$Fe$_{0.8}$O$_{3-\delta}$	122 185 236	600 650 700	1.06 1.03 1.00	[68]
Ni-BaZr$_{0.1}$Ce$_{0.7}$Y$_{0.2}$O$_{3-\delta}$ (BZCY) ‖BZCY‖BaZr$_{0.8}$Y$_{0.2}$O$_{3-\delta}$ (BZY) ‖La$_{0.6}$Sr$_{0.4}$Co$_{0.2}$Fe$_{0.8}$O$_{3-\delta}$ (LSCF)-BZY	74 131 181	600 650 700	1.01 1.00 0.98	[69]

1 * Indicates the value estimated from the graph

2 *Scanning electron microscopy*

3
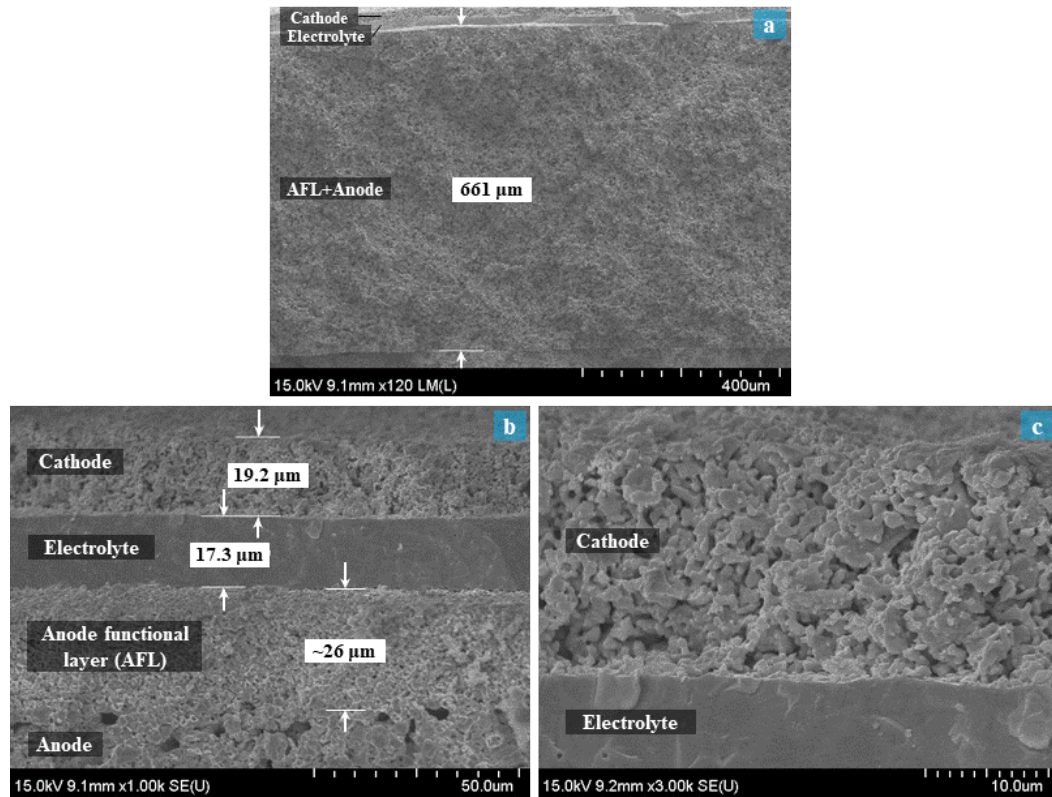
5 **Fig. 9** SEM cross-sectional image of the BSCF | BSCZYSm | Ni-BSCZYSm fuel cell at

6 magnifications of a) 120, b) 1,000 and c) 3,000.

7

Microstructure plays a very important role in the properties of materials [70]. More importantly, in the case of a fuel cell, we need to optimize the dense electrolyte and porous electrodes. Electrolytes need to be gas tight to prevent the mixing of gaseous reactants. In proton-conducting oxides, grain boundary resistance is detrimental to the total conductivity, and an increase in the grain size decreases the number of grain boundaries, which obviously results in a reduction in grain boundary resistance and hence an increase in the total ionic conductivity. Fig. 9a) –c) show the SEM cross-section images of the Ni-BSCZYSm | BSCZYSm | BSCF fuel cell with a total thickness of 697.5 μm. The cathode and anode appear as porous layers with a dense electrolyte layer. The cathode and electrolyte layers were attached well with no delamination, which demonstrates the good chemical compatibility and stability of the cathode-electrolyte layer at the deposition temperature of 1,000 °C, and the compatibility of these two layers was examined by XRD (see Fig. 2). The electrolyte membrane exhibited a dense microstructure with no visible cracks or holes, which confirms the prevention of fuel cross-over from the anode and oxidant from the cathode. In this study, the drop coating of the electrolyte onto the anode was sufficient to achieve a thickness of ~17 μm. Even though the electrolyte thickness is slightly higher than those reported by Ding et al. [56], [57] and He et al. [69], the achieved performance is higher than those of similar electrolyte-based fuel cells.

Conclusions

A proton-conducting perovskite electrolyte, $Ba_{0.9}Sr_{0.1}Ce_{0.5}Zr_{0.35}Y_{0.1}Sm_{0.05}O_{3-\delta}$ (BSCZYSm), exhibited unique characteristics in fuel cell application, showing a high power density at intermediate temperatures. BSCZYSm showed cubic symmetry in the *Pm-3m* space group and good proton conductivity. BSCZYSm was successfully synthesized by using a solid-state sintering method with microscale particle sizes. The oxygen deficiency was determined by TGA and was consistent with the theoretical value, showing the potential to achieve good ionic conductivity. The proton conductivity of BSCZYSm was 4.167×10^{-3} S cm^{-1} at 700 °C in a wet argon atmosphere, which is higher than those of other similar proton conductors. BSCZYSm was utilized as an electrolyte layer in the fuel cell in the $NiO-Ba_{0.9}Sr_{0.1}Ce_{0.5}Zr_{0.35}Y_{0.1}Sm_{0.05}O_{3-\delta}$ (BSCZYSm)‖BSCZYSm‖$Ba_{0.5}Sr_{0.5}Co_{0.8}Fe_{0.2}O_{3-\delta}$ arrangement. The cell exhibited a peak power density of 581.7 mW/cm^2 at 700 °C as a proton-conducting fuel cell, which was confirmed by the presence of condensed water at the cathode outlet. The OCV of the fuel cell at 700 °C was

1.025 V, which was higher at a lower temperature, as predicted by the Nernst equation. Notably, we have used only one device technology to obtain results. Different cell arrangements can be employed to achieve even better performance.

Acknowledgements

Author contributions

A.K.A. got the idea, designed the experiments and supervised the project. N.R. did the sample preparation, characterization and prepared the first draft. A.A. and A.M.A. helped during XRD and SEM experiments and refinement. M.S. and J.Y.P. helped to prepare fuel cell and test. J.Z., J.I. and J.H.K. have supervised the project, helped to write the manuscript and to edit it.

Competing interest

There is no competing interest in this work.

Materials & Correspondence

For correspondence and materials request, please contact Dr. Abul Kalam Azad, Faculty of Integrated Technologies, Jalan Tungku Link, Gadong, BE 1410, Brunei Darussalam. Email: abul.azad@ubd.edu.bn, Phone: +6737219025

References

[1]   A. M. Abdalla, S. Hossain, A. T. Azad, P. M. I. Petra, F. Begum, S. G. Eriksson, A. K. Azad, *Renew. Sustain. Energy Rev.* **2018**, *82*, *Part 1*, 353–368.

[2]   S. Park, J. M. Vohs, R. J. Gorte, *Nature* **2000**, *404*, 265–267.

[3]   N. Radenahmad, A. Afif, P. I. Petra, S. M. H. Rahman, S.-G. Eriksson, A. K. Azad,

Renew. Sustain. Energy Rev. **2016**, *57*, 1347–1358.

[4] N. Radenahmad, A. Afif, M. I. Petra, S. M. H. Rahman, S. Eriksson, A. K. Azad, *Int. J. Hydrogen Energy* **2016**, *41*, 11832–11841.

[5] D. Medvedev, A. Murashkina, E. Pikalova, A. Demin, A. Podias, P. Tsiakaras, *Prog. Mater. Sci.* **2014**, *60*, 72–129.

[6] S. Hossain, A. M. Abdalla, S. N. B. Jamain, J. H. Zaini, A. K. Azad, *Renew. Sustain. Energy Rev.* **2017**, *79*, 750–764.

[7] R. J. Gorte, *Sci.* **2015**, *349*, 1290.

[8] C. Xia, Y. Mi, B. Wang, B. Lin, G. Chen, B. Zhu, *Nat. Commun.* **2019**, *10*, 1707.

[9] Z. Shi, W. Sun, W. Liu, *J. Power Sources* **2014**, *245*, 953–957.

[10] H. Iwahara, T. Esaka, H. Uchida, N. Maeda, *Solid State Ionics* **1981**, *3–4*, 359–363.

[11] M. Naeem Khan, C. D. Savaniu, A. K. Azad, P. Hing, J. T. S. Irvine, *Solid State Ionics* **2017**, *303*, 52–57.

[12] A. Afif, N. Radenahmad, C. M. Lim, M. I. Petra, M. A. Islam, S. M. H. Rahman, S. Eriksson, A. K. Azad, *Int. J. Hydrogen Energy* **2016**, *41*, 11823–11831.

[13] A. M. Abdalla, S. Hossain, J. Zhou, P. M. I. Petra, S. Erikson, C. D. Savaniu, J. T. S. Irvine, A. K. Azad, *Ceram. Int.* **2017**, *43*, 15932–15938.

[14] A. K. Azad, J. T. S. Irvine, *Solid State Ionics* **2008**, *179*, 678–682.

[15] S. Hossain, A. M. Abdalla, N. Radenahmad, A. K. M. Zakaria, J. H. Zaini, S. M. H. Rahman, S. G. Eriksson, J. T. S. Irvine, A. K. Azad, *Int. J. Hydrogen Energy* **2018**, *43*, 894–907.

[16] S. Tao, J. T. S. Irvine, *Adv. Mater.* **2006**, *18*, 1581–1584.

[17] A. K. Azad, A. Kruth, J. T. S. Irvine, *Int. J. Hydrogen Energy* **2014**, *39*, 12804–12811.

[18] A. K. Azad, J. T. S. Irvine, *Solid State Ionics* **2007**, *178*, 635–640.

[19] N. Radenahmad, A. Afif, P. I. Petra, S. M. H. Rahman, S.-G. Eriksson, A. K. Azad, *Renew. Sustain. Energy Rev.* **2016**, *57*, 1347–1358.

[20] Z. Tao, Z. Zhu, H. Wang, W. Liu, *J. Power Sources* **2010**, *195*, 3481–3484.

[21]   L. Yang, S. Wang, K. Blinn, M. Liu, Z. Liu, Z. Cheng, M. Liu, *Science* **2009**, *326*, 126–129.

[22]   E. Fabbri, A. Depifanio, E. Dibartolomeo, S. Licoccia, E. Traversa, *Solid State Ionics* **2008**, *179*, 558–564.

[23]   K. Katahira, Y. Kohchi, T. Shimura, H. Iwahara, *Solid State Ionics* **2000**, *138*, 91–98.

[24]   Y. Liu, L. Yang, M. Liu, Z. Tang, M. Liu, *J. Power Sources* **2011**, *196*, 9980–9984.

[25]   S. Ricote, N. Bonanos, G. Caboche, *Solid State Ionics* **2009**, *180*, 990–997.

[26]   I.-M. Hung, H.-W. Peng, S.-L. Zheng, C.-P. Lin, J.-S. Wu, *J. Power Sources* **2009**, *193*, 155–159.

[27]   W. Araki, Y. Arai, J. Malzbender, *Mater. Lett.* **2014**, *132*, 295–297.

[28]   Z. Shao, S. M. Haile, *Nature* **2004**, *431*, 170–173.

[29]   J. Rodriguez-Carvajal, *Phys. B Condens. Matter* **1993**, *192*, 55.

[30]   J. Wu, R. a. Davies, M. S. Islam, S. M. Haile, *Chem. Mater.* **2005**, *17*, 846–851.

[31]   R. L. Moreira, A. Dias, *J. Phys. Chem. Solids* **2007**, *68*, 1617–1622.

[32]   Z. Shi, W. Sun, Z. Wang, J. Qian, W. Liu, *ACS Appl. Mater. Interfaces* **2014**, *6*, 5175–82.

[33]   A. K. Azad, J. T. S. Irvine, *Chem. Mater.* **2009**, *21*, 215–222.

[34]   A. Braun, Q. Chen, *Nat. Commun.* **2017**, *8*, 15830.

[35]   N. Agmon, *Chem. Phys. Lett.* **1995**, *244*, 456–462.

[36]   M. S. Islam, P. R. Slater, J. R. Tolchard, T. Dinges, *Dalt. Trans.* **2004**, 3061–3066.

[37]   K. R. Lee, C. J. Tseng, J. K. Chang, I. M. Hung, J. C. Lin, S. W. Lee, *Int. J. Hydrogen Energy* **2013**, *38*, 11097–11103.

[38]   S. K. Jaiswal, S. M. Choi, K. J. Yoon, J. W. Son, B. K. Kim, H. W. Lee, J. H. Lee, *Int. J. Hydrogen Energy* **2015**, *40*, 11022–11031.

[39]   Y.-C. Liou, S.-L. Yang, *J. Power Sources* **2008**, *179*, 553–559.

[40]   A. Afif, N. Radenahmad, C. M. Lim, Q. Cheok, A. Islam, S. M. H. Rahman, A. K. Azad, *IOP Conf. Ser. Mater. Sci. Eng.* **2016**, *121*, 012006.

1   [41] A. Satapathy, E. Sinha, *J. Alloys Compd.* **2019**, *772*, 675–682.

2   [42] T. H. Lee, K. Y. Park, N. I. Kim, S. J. Song, K. H. Hong, D. Ahn, A. K. Azad, J. Hwang,
3   S. Bhattacharjee, S. C. Lee, H. T. Lim, J. Y. Park, *J. Power Sources* **2016**, *331*, 495–506.

4   [43] Y. Li, S. Wang, P.-C. Su, *Sci. Rep.* **2016**, *6*, 22369.

5   [44] B. Wang, L. Bi, X. S. Zhao, *J. Power Sources* **2018**, *399*, 207–214.

6   [45] C. Peng, J. Melnik, J. Li, J. Luo, A. R. Sanger, K. T. Chuang, *J. Power Sources* **2009**, *190*,
7   447–452.

8   [46] W. Sun, Y. Wang, S. Fang, Z. Zhu, L. Yan, W. Liu, *Electrochim. Acta* **2011**, *56*, 1447–
9   1454.

10 [47] A. R. Hanifi, N. K. Sandhu, T. H. Etsell, J.-L. Luo, P. Sarkar, *J. Power Sources* **2017**, *341*,
11   264–269.

12 [48] Z. Zhu, E. Guo, Z. Wei, H. Wang, *J. Power Sources* **2018**, *373*, 132–138.

13 [49] X. Xu, H. Wang, M. Fronzi, X. Wang, L. Bi, E. Traversa, *J. Mater. Chem. A* **2019**, *7*,
14   20624–20632.

15 [50] J. Ma, Z. Tao, H. Kou, M. Fronzi, L. Bi, *Ceram. Int.* **2020**, *46*, 4000–4005.

16 [51] X. Xu, H. Wang, J. Ma, W. Liu, X. Wang, M. Fronzi, L. Bi, *J. Mater. Chem. A* **2019**, *7*,
17   18792–18798.

18 [52] N. T. Q. Nguyen, H. H. Yoon, *J. Power Sources* **2013**, *231*, 213–218.

19 [53] J. Li, C. Wang, X. Wang, L. Bi, *Electrochem. commun.* **2020**, *112*, 106672.

20 [54] F. Zhao, S. Wang, L. Dixon, F. Chen, *J. Power Sources* **2011**, *196*, 7500–7504.

21 [55] F. Zhao, C. Jin, C. Yang, S. Wang, F. Chen, *J. Power Sources* **2011**, *196*, 688–691.

22 [56] H. Ding, Y. Xie, X. Xue, *J. Power Sources* **2011**, *196*, 2602–2607.

23 [57] H. Ding, X. Xue, *J. Power Sources* **2010**, *195*, 7038–7041.

24 [58] H. Gu, Y. Zheng, R. Ran, Z. Shao, W. Jin, N. Xu, J. Ahn, *J. Power Sources* **2008**, *183*,
25   471–478.

26 [59] S. Zhang, L. Bi, L. Zhang, Z. Tao, W. Sun, H. Wang, W. Liu, *J. Power Sources* **2009**,
27   *188*, 343–346.

1   [60]   H. Ding, X. Xue, X. Liu, G. Meng, *J. Alloys Compd.* **2010**, *494*, 233–235.

2   [61]   M. Jin, X. Zhang, Y. Qiu, J. Sheng, *J. Alloys Compd.* **2010**, *494*, 359–361.

3   [62]   X. Lu, Y. Ding, Y. Chen, *J. Alloys Compd.* **2009**, *484*, 856–859.

4   [63]   H. Ding, B. Lin, X. Liu, G. Meng, *Electrochem. commun.* **2008**, *10*, 1388–1391.

5   [64]   X. Zhang, M. Jin, J. Sheng, *J. Alloys Compd.* **2010**, *496*, 241–243.

6   [65]   Y. Li, R. Guo, C. Wang, Y. Liu, Z. Shao, J. An, C. Liu, *Electrochim. Acta* **2013**, *95*, 95–
7   101.

8   [66]   J. Xu, X. Lu, Y. Ding, Y. Chen, *J. Alloys Compd.* **2009**, *488*, 208–210.

9   [67]   B. Lin, Y. Dong, S. Wang, D. Fang, H. Ding, X. Zhang, X. Liu, G. Meng, *J. Alloys*
10   *Compd.* **2009**, *478*, 590–593.

11 [68]   B. Lin, M. Hu, J. Ma, Y. Jiang, S. Tao, G. Meng, *J. Power Sources* **2008**, *183*, 479–484.

12 [69]   B. He, D. Ding, Y. Ling, L. Zhao, J. Cheng, *Int. J. Hydrogen Energy* **2014**, *39*, 19087–
13   19092.

14 [70]   Y. Zhang, Z. Su, A. K. Azad, W. Zhou, J. T. S. Irvine, *Adv. Energy Mater.* **2012**, *2*, 316–
15   321.

16

17

18